On the Performance of Discretization and Trust-Region Methods for Onboard Convex Low-Thrust Trajectory Optimization

Christian Hofmann*, Andrea C. Morelli† and Francesco Topputo‡
Politecnico di Milano, Milan, Italy, 20156

Different discretization and trust-region methods are assessed and compared for the low-thrust fuel-optimal trajectory optimization problem using successive convex programming. In particular, the differential and integral formulations of the adaptive pseudospectral Legendre–Gauss–Radau method, an arbitrary-order Legendre–Gauss–Lobatto technique based on Hermite interpolation, and a first-order-hold discretization are considered. The number of nodes and segments is varied, and the suitability for onboard guidance is assessed. Moreover, two hard trust-region methods and a soft trust-region strategy are compared. A perturbed cubic interpolation and the propagation of the nonlinear dynamics with tangential thrust are used to generate initial guesses of varying quality and to evaluate the performance. Interplanetary transfers to a near-Earth asteroid, Venus, and asteroid Dionysus are chosen to assess the overall performance.

I. Introduction

The number of new space missions has grown rapidly, especially interplanetary CubeSats are becoming increasingly important as the success of NASA's MarCO mission has shown [1]. Their low development costs make them an appealing option for many missions. Even though the computational capability of onboard computers has increased continuously in the past years, only minor advances in the guidance and control systems have taken place. It is therefore not surprising that a paradigm shift is currently happening [2]. Rather than calculating the guidance and control actions on ground, these tasks shall be performed onboard. This is not only crucial for more autonomous and safer systems, but also of paramount importance to reduce the operational costs even further [3]. As the computational capability of onboard computers has increased continuously in the past years, real-time guidance seems to become reality as already demonstrated in flight tests of the Masten Space Systems Xombie suborbital rocket [4]. Instead of aiming at a closed-form solution, numerical algorithms are sought to iteratively compute feasible trajectories on spacecraft hardware.

Even though feasibility is often sufficient for many applications, minimum fuel consumption is of utmost importance for space flight. The costs to launch a satellite still amount to several thousand dollars per kilogram, and decreasing the launch mass can contribute to reducing the overall mission cost [5]. In addition, spacecraft (especially CubeSats) have severe limitations regarding the propellant mass. Therefore, it is desirable to not only compute feasible, but also (near-)optimal trajectories. This, however, requires solving a nonlinear optimal control problem. Direct and indirect methods are most commonly used to find a solution [6]. Given the requirements for onboard applications, such as high robustness and reliability, indirect methods play a rather secondary role, often due to the small convergence domain [7]. Moreover, as the number of revolutions for interplanetary transfers is relatively small, the need for indirect methods becomes less significant as only a relatively small number of discretization points is often sufficient to capture the trajectories accurately. On the contrary, the recent developments of convex programming techniques have made direct methods a promising approach for real-time guidance [8–10]. The successive optimization method allows solving nonconvex optimal control problems with nonlinear dynamics and constraints, therefore being a viable alternative for many aerospace applications such as powered descent guidance (PDG) and low-thrust trajectory optimization (LTO) [11–13]. Solving a series of simpler, convex subproblems makes this method numerically tractable compared to solving a nonlinear program directly. Two key characteristics of this so-called sequential convex programming technique (SCP) are the discretization and trust-region methods; they strongly affect the results, especially the convergence

*Ph.D. Candidate, Department of Aerospace Science and Technology, Via La Masa 34, 20156 Milan, Italy. Email: christian.hofmann@polimi.it.
†Ph.D. Candidate, Department of Aerospace Science and Technology, Via La Masa 34, 20156 Milan, Italy. Email: andreacarlo.morelli@polimi.it.
‡Professor, Department of Aerospace Science and Technology, Via La Masa 34, 20156 Milan, Italy. Email: francesco.topputo@polimi.it.

properties. Yet, previous research activities lack a thorough assessment and comparison of relevant techniques for onboard low-thrust trajectory optimization.

The most popular discretization techniques are collocation and control interpolation methods. The former parameterize both the states and controls using some basis functions, whereas the latter parameterize only the control history [6]. Due to its simplicity, the trapezoidal rule is one of the most important collocation methods [14, 15]. Yet, its poor accuracy often prevents the solver to find solutions that satisfy the nonlinear dynamics for long-duration interplanetary transfers. Higher-order methods such as Hermite–Simpson collocation offer instead a good compromise between computational effort and accuracy [16]. The arbitrary-order Hermite–Legendre–Gauss–Lobatto discretization is a generalization of this method and a popular choice in nonlinear optimization as it allows approximating the states with higher-order Hermite interpolating polynomials [17]. In global pseudospectral methods, in contrast, single Lagrange interpolating polynomials are used to approximate the states and controls, respectively. As this results in dense matrices, adaptive methods were developed where piecewise polynomials are used to approximate the trajectories [18]. Moreover, it was shown that using a non-uniform temporal grid where the nodes are defined as the roots of an orthogonal Legendre polynomial is often advantageous [19]. The reason is that the accuracy of approximating integrals using orthogonal collocation points is higher compared to non-orthogonal collocation. There are several categories of pseudospectral methods; the most important ones are based on Legendre–Gauss–Lobatto [17], Legendre–Gauss [20], or Legendre–Gauss–Radau points [21]. Several works adapted these methods to convex programming and solved powered descent and low-thrust guidance problems [12, 13, 22–24]. With regard to control interpolation methods, the control is approximated using a zero-order-hold (ZOH) or first-order-hold (FOH) discretization. For ZOH, the control history is assumed piecewise constant, whereas for FOH, it is approximated as a piecewise affine function [25]. Both methods performed well for powered descent guidance problems [11, 25]. The ZOH discretization was also applied successfully to low-thrust trajectory optimization problems in the circular restricted three-body problem [26].

We want to note that the work in [27] compares different discretization methods (namely ZOH, FOH, classical Runge-Kutta methods, and three global pseudospectral methods) for the PDG problem. However, the results cannot be applied directly to the low-thrust trajectory optimization problem due to the different dynamics, constraints, and discontinuous control structure. One major difference is that the time horizon is considerably shorter in PDG compared to the long-duration interplanetary transfers in LTO which can last several years. Therefore, many more nodes are required to capture the state and control profiles accurately, especially if the number of revolutions increases. A global pseudospectral method using only one high-order polynomial as in [27] would result in dense matrices and a considerable higher solving time (if a solution is found at all). Hence, an adaptive strategy as in [12] is needed for the LTO problem. In this work, we choose the differential and integral formulations of an adaptive pseudospectral method based on the standard and flipped Legendre–Gauss–Radau points; these seem to be a natural choice in an adaptive framework due to the definition of the collocation points. In addition, a recently developed arbitrary-order Legendre–Gauss–Lobatto method [13] and the control interpolation technique FOH are compared. We believe that this selection covers the most important and relevant discretization methods for solving the LTO problem.

The second part of this paper assesses different trust-region methods. Trust regions are imposed to keep the linearization close to a reference solution. All of the SCP methods found in literature use some type of trust-region approach. For powered descent guidance problems, soft trust regions (where the constraint is penalized in the cost function) are often used [25, 28]. In low-thrust trajectory optimization, simple hard trust regions (where the trust-region constraint is imposed directly) are more common [12, 29]. The choice of the trust-region approach is often crucial as this can decide whether a feasible solution is found or not. Furthermore, a poor choice of the parameters can deteriorate the convergence. Such a behavior is undesirable and unacceptable for onboard applications. Soft trust regions often work well in powered descent guidance problems, but they have not been used to determine low-thrust trajectories so far. None of the existing works has investigated how different trust-region methods affect the performance of the SCP algorithm for complex interplanetary low-thrust fuel-optimal transfers. Moreover, no conclusion can be drawn on how the choice might affect the real-time capability of the algorithm. For this reason, we compare the performance of two different hard (standard and adaptive formulation) and one soft trust-region method. The performance is assessed in transfers to the near-Earth asteroid (NEA) 2000 SG344, Venus, and asteroid Dionysus.

The paper is structured as follows. Section II states the optimal control problem and the convexification. Section III describes the discretization methods, and Section IV presents the trust-region methods. The results are presented and discussed in Section V. Section VI concludes this paper.

II. Problem Formulation

The motion of a spacecraft around a primary body is governed by the dynamics

$$\dot{\mathbf{r}}(t) = \mathbf{v}(t) \tag{1}$$

$$\dot{\mathbf{v}}(t) = -\frac{\mu\,\mathbf{r}(t)}{r(t)^3} + \frac{\mathbf{T}(t)}{m(t)} \tag{2}$$

$$\dot{m}(t) = -\frac{\|\mathbf{T}(t)\|_2}{g_0\, I_{\text{sp}}} \tag{3}$$

where $\mathbf{r}(t) \in \mathbb{R}^{3\times1}$, $\mathbf{v}(t) \in \mathbb{R}^{3\times1}$, and $m(t) \in \mathbb{R}$ denote the position, velocity, and mass of the spacecraft, respectively. μ is the gravitational parameter of the primary body and g_0 denotes the gravitational acceleration at sea level. The control actions are governed by the thrust components $\mathbf{T}(t) \in \mathbb{R}^{3\times1}$, $I_{\text{sp}} \in \mathbb{R}$ being the specific impulse.
We seek to minimize fuel usage, which is equivalent to maximizing the mass at the final time t_f:

$$\underset{\mathbf{T}(t)}{\text{minimize}} \quad -m(t_f) \tag{4}$$

In this work, we intend to target a specific point $\left[\mathbf{r}_f^\top, \mathbf{v}_f^\top\right]^\top$ in space. Therefore, the prescribed boundary conditions at the initial t_0 and final times are

$$\mathbf{r}(t_0) = \mathbf{r}_0, \quad \mathbf{v}(t_0) = \mathbf{v}_0, \quad m(t_0) = m_0 \tag{5}$$

$$\mathbf{r}(t_f) = \mathbf{r}_f, \quad \mathbf{v}(t_f) = \mathbf{v}_f \tag{6}$$

where the value of the final mass is free. As the engine can provide only limited thrust, the following lower and upper bounds on the thrust magnitude need to be imposed:

$$0 \le T_{\min} \le \|\mathbf{T}(t)\|_2 \le T_{\max} \tag{7}$$

with the minimum $T_{\min}$ and maximum $T_{\max}$ available thrust magnitudes. Note that we use $T_{\min} = 0$ throughout this paper. The nonlinear part $\mathbf{T}(t)/m(t)$ in Eq. (2) is eliminated by a change of variables [11]:

$$\Gamma(t) \coloneqq \frac{\|\mathbf{T}(t)\|_2}{m(t)}, \quad \boldsymbol{\tau}(t) \coloneqq \frac{\mathbf{T}(t)}{m(t)}, \quad z(t) \coloneqq \ln m(t) \tag{8}$$

As the thrust constraint in Eq. (7) becomes nonconvex now, it is linearized about the reference $\bar{z}$:

$$0 \le \Gamma(t) \le T_{\max} e^{-\bar{z}}\,(1 - z(t) + \bar{z}(t)) \tag{9}$$

Defining the states and controls as $\mathbf{x} = [\mathbf{r}^\top, \mathbf{v}^\top, z]^\top$ and $\mathbf{u} = [\boldsymbol{\tau}^\top, \Gamma]^\top$, respectively, the new dynamics are

$$\dot{\mathbf{x}}(t) = \mathbf{f}(\mathbf{x}(t), \mathbf{u}(t)) = \begin{bmatrix} \mathbf{v}(t) \\ -\mu\,\mathbf{r}(t)/r(t)^3 + \boldsymbol{\tau}(t) \\ -\Gamma(t)/(g_0\, I_{\text{sp}}) \end{bmatrix} \tag{10}$$

Linearizing Eq. (10) about a reference solution $\bar{\mathbf{x}}$ and adding a trust-region constraint to keep the linearization valid, the convexified optimization problem is stated as follows:

$$\begin{aligned}
&\underset{\mathbf{u}(t)}{\text{minimize}} && -z(t_f) + \lambda\, \|\boldsymbol{\nu}(t)\|_1 + \lambda\, \max(0, \eta(t)) && \text{(11a)}\\
&\text{subject to:} && \dot{\mathbf{x}}(t) = \mathbf{A}(\bar{\mathbf{x}}(t))\,\mathbf{x}(t) + \mathbf{B}\mathbf{u}(t) + \mathbf{q}(\bar{\mathbf{x}}(t), \bar{\mathbf{u}}(t)) + \boldsymbol{\nu}(t) && \text{(11b)}\\
& && \Gamma(t) \le T_{\max} e^{-\bar{z}(t)}\,(1 - z(t) + \bar{z}(t)) + \eta(t) && \text{(11c)}\\
& && \|\mathbf{x}(t) - \bar{\mathbf{x}}(t)\|_1 \le R && \text{(11d)}\\
& && \mathbf{r}(t_0) = \mathbf{r}_0,\ \mathbf{v}(t_0) = \mathbf{v}_0,\ z(t_0) = z_0 && \text{(11e)}\\
& && \mathbf{r}(t_f) = \mathbf{r}_f,\ \mathbf{v}(t_f) = \mathbf{v}_f && \text{(11f)}
\end{aligned}$$

where

$$\mathbf{A}(\bar{\mathbf{x}}(t)) \coloneqq \left.\frac{\partial \mathbf{f}}{\partial \mathbf{x}}\right|_{\bar{\mathbf{x}}(t)}, \ \mathbf{B} \coloneqq \left.\frac{\partial \mathbf{f}}{\partial \mathbf{u}}\right|_{\bar{\mathbf{u}}(t)}, \ \mathbf{q}(\bar{\mathbf{x}}(t), \bar{\mathbf{u}}(t)) \coloneqq \mathbf{f}(\bar{\mathbf{x}}(t), \bar{\mathbf{u}}(t)) - \mathbf{A}(\bar{\mathbf{x}}(t))\,\bar{\mathbf{x}}(t) - \mathbf{B}\bar{\mathbf{u}}(t) \tag{12}$$

Note that Eqs. (11b) and (11c) are augmented with slack variables $\boldsymbol{\nu}(t)$ and $\eta(t) \ge 0$ to avoid artificial infeasibility. They are penalized in the cost function in Eq. (11a) with a sufficiently large parameter $\lambda > 0$. The trust-region constraint in Eq. (11d) with radius R is imposed to keep the linearization close to the reference.

III. Discretization Methods

We consider the following discretization methods in this work:

1) An adaptive Legendre–Gauss–Radau pseudospectral method (RPM).
2) An arbitrary-order Legendre–Gauss–Lobatto method (LGL) based on Hermite interpolation.
3) A first-order-hold discretization.

The RPM has demonstrated to perform well for nonlinear programs and also low-thrust trajectory design within convex programming [12, 18]. Moreover, as either the initial or final point is not collocated, it seems to be an appropriate choice for an adaptive framework as there is no redundancy or even lack of nodes between consecutive segments compared to other pseudospectral methods that are based on Legendre–Gauss or Legendre–Gauss–Lobatto points [30]. We also consider the arbitrary-order Legendre–Gauss–Lobatto method based on Hermite interpolation as it is a generalization of the well-known Hermite-Simpson collocation. It therefore covers a wide range of methods that have proven effective to solve nonlinear programs [31]. FOH is chosen as it belongs to the class of control interpolation techniques. Note that we do not consider a zero-order-hold discretization as a piecewise constant approximation of the acceleration would result in a poor approximation of the thrust profile.

A. Adaptive Legendre–Gauss–Radau Pseudospectral Method

In an adaptive pseudospectral method, the trajectory is divided into K segments and the states and controls are approximated using Lagrange interpolating polynomials of different degrees. The collocation points are defined as the roots of the polynomial $P_{N-1}(\xi) + P_N(\xi)$ where P_N is the Nth degree Legendre polynomial. These points are defined in the pseudospectral time domain $\xi \in [-1, 1]$. The transformation between the physical t and pseudospectral time is given by [32]

$$t_i^{(k)} = t_{N_k}^{(k-1)} + \frac{t_{N_k}^{(k)} - t_0^{(k)}}{2}\xi_i^{(k)} + \frac{t_{N_k}^{(k)} + t_0^{(k)}}{2} \qquad i = 0, 1, ..., N_k \tag{13}$$

with $t_{N_k}^{(0)} = 0$. Throughout this section, the number of collocation points per segment (and hence, the degree of the interpolating polynomial) is denoted as N_k, and $\mathbf{x}_i^{(k)}$, $\mathbf{u}_i^{(k)}$ refer to the ith point of the kth segment of states and controls at time $t_i^{(k)}$, with $i = 0, 1, ..., N_k$ and $k = 1, ..., K$. The states and controls are approximated in the interval $[-1, 1]$ as follows:

$$\mathbf{x}^{(k)}(\xi) = \sum_{i=0}^{N_k} \mathbf{x}_i^{(k)} L_i^{(k)}(\xi), \qquad \mathbf{u}^{(k)}(\xi) = \sum_{i=0}^{N_k} \mathbf{u}_i^{(k)} L_i^{(k)}(\xi) \tag{14}$$

with

$$L_i^{(k)}(\xi) = \prod_{\substack{j=0 \\ j\neq i}}^{N_k} \frac{\xi - \xi_j}{\xi_i - \xi_j} \tag{15}$$

Depending on the chosen method, the initial or final point may or may not be included in the interpolation. The basic idea of pseudospectral methods is to approximate the differential operator as $\dot{\mathbf{x}}^{(k)} \approx \mathbf{D}^{(k)}\mathbf{x}^{(k)}$ where $\mathbf{D}^{(k)} \in \mathbb{R}^{N_k \times (N_k+1)}$ is a non-square differentiation matrix whose elements are defined as $D_{ij} := L_j'(\xi_i)$ [33].

This work presents two formulations of the Radau pseudospectral method:

1) A Radau pseudospectral method using the standard Legendre–Gauss–Radau (LGR) points.
2) A flipped Radau pseudospectral method (FRPM) using the flipped LGR points

We dedicate individual sections to each method as they differ in several aspects. We consider the differential and integral formulations of each method. The interested reader is referred to [34] and [12, 35] for details on RPM and FRPM, respectively.

1. Adaptive Radau Pseudospectral Method

The dynamics are approximated at the LGR points defined on $[-1, 1)$. Therefore, the last node of each segment is not a collocation point, but it is used to approximate the state. Note, however, that the final control $\mathbf{u}_{N_K}^{(K)}$ is not obtained in the solution process and must therefore be determined by extrapolation. Using the differentiation matrix $\mathbf{D}^{(k)}$, the dynamics can be written in differential form as follows:

$$\begin{aligned}\sum_{j=0}^{N_k} D_{ij}^{(k)} \mathbf{x}_j^{(k)} &= \frac{t_{N_k}^{(k)} - t_0^{(k)}}{2} \mathbf{f}(\mathbf{x}_i^{(k)}, \mathbf{u}_i^{(k)}) \\ &= \frac{t_{N_k}^{(k)} - t_0^{(k)}}{2} \left[\mathbf{A}(\bar{\mathbf{x}}_{\mathbf{i}}^{(\mathbf{k})}) \mathbf{x}_i^{(k)} + \mathbf{B}\mathbf{u}_i^{(k)} + \mathbf{q}(\bar{\mathbf{x}}_i^{(k)}) + \boldsymbol{\nu}_i^{(k)} \right], \qquad i = 0, 1, ..., N_k - 1\end{aligned} \tag{16}$$

The factor $\Delta := \frac{t_{N_k}^{(k)} - t_0^{(k)}}{2}$ is needed due to the time transformation from the physical time to $[-1, 1]$. As the final point of each segment is not collocated, the linking condition $\mathbf{x}_{N_k}^{(k)} = \mathbf{x}_0^{(k+1)}$ must hold for segments $k < K$. The dynamics can then be written in standard form as a linear equality constraint:

$$\left[\begin{array}{ccc:ccc:ccc} \hat{\mathbf{A}}^{(1)} & & \mathbf{0} & \hat{\mathbf{B}}^{(1)} & & \mathbf{0} & \mathbf{1}^{(1)} & & \mathbf{0} \\ & \ddots & & & \ddots & & & \ddots & \\ \mathbf{0} & & \hat{\mathbf{A}}^{(K)} & \mathbf{0} & & \hat{\mathbf{B}}^{(K)} & \mathbf{0} & & \mathbf{1}^{(K)} \end{array}\right] \cdot \begin{bmatrix} \mathbf{X} \\ \mathbf{U} \\ \boldsymbol{\nu} \end{bmatrix} = \begin{bmatrix} \hat{\mathbf{q}}^{(1)} \\ \vdots \\ \hat{\mathbf{q}}^{(K)} \end{bmatrix} \tag{17}$$

where the matrices $\hat{\mathbf{A}}^{(k)}$ and $\hat{\mathbf{B}}^{(k)}$ are calculated using $\mathbf{D}^{(k)}$ and the Jacobian matrices defined in Eq. (12). $\mathbf{1}^{(k)}$ are identity matrices and $\hat{\mathbf{q}}^{(k)}$ are comprised of the constant parts of the linearization. $\mathbf{X}$, $\mathbf{U}$, and $\boldsymbol{\nu}$ denote the concatenated states, controls, and virtual controls, respectively. The $\hat{\mathbf{A}}^{(k)}$ take the following form

$$\hat{\mathbf{A}}^{(k)} = \begin{bmatrix} D_{00}\,\mathbf{1} - \Delta\,\mathbf{A}_0 & D_{01}\,\mathbf{1} & \dots & D_{0,N_k-1}\,\mathbf{1} & D_{0,N_k}\,\mathbf{1} \\ D_{10}\,\mathbf{1} & D_{11}\,\mathbf{1} - \Delta\,\mathbf{A}_1 & \dots & D_{1,N_k-1}\,\mathbf{1} & D_{1,N_k}\,\mathbf{1} \\ \vdots & \vdots & \ddots & \vdots & \vdots \\ D_{N_k-1,0}\,\mathbf{1} & & \dots & D_{N_k-1,N_k-1}\,\mathbf{1} - \Delta\,\mathbf{A}_{N_k-1} & D_{N_k-1,N_k}\,\mathbf{1} \end{bmatrix} \tag{18}$$

where we omitted $(\cdot)^{(k)}$ for the sake of conciseness. $\hat{\mathbf{B}}^{(k)}$ are diagonal matrices with entries $-\Delta\,\mathbf{B}_i$, and $\hat{\mathbf{q}}^{(k)}$ is a concatenated vector where the elements take the form $\Delta\,\mathbf{q}_i$.
It was observed that an equivalent integral formulation of Eq. (16) may yield more consistent results [36]. Defining an integration matrix $\mathbf{I} \in \mathbb{R}^{N_k \times N_k}$ as $\mathbf{I} := \mathbf{D}_{1:N_k}^{-1}$ where $\mathbf{D}_{1:N_k}$ is obtained by removing the first column of $\mathbf{D}$, the dynamics are

$$\begin{aligned}\mathbf{x}_{i+1}^{(k)} &= \mathbf{x}_0^{(k)} + \frac{t_{N_k}^{(k)} - t_0^{(k)}}{2} \sum_{j=0}^{N_k-1} I_{ij}^{(k)} \mathbf{f}(\mathbf{x}_j^{(k)}, \mathbf{u}_j^{(k)}) \\ &= \mathbf{x}_0^{(k)} + \frac{t_{N_k}^{(k)} - t_0^{(k)}}{2} \sum_{j=0}^{N_k-1} I_{ij}^{(k)} \left[\mathbf{A}(\bar{\mathbf{x}}_j^{(k)}) \mathbf{x}_j^{(k)} + \mathbf{B}\mathbf{u}_j^{(k)} + \mathbf{q}(\bar{\mathbf{x}}_j^{(k)}) + \boldsymbol{\nu}_j^{(k)} \right] \qquad i = 0, ..., N_k - 1\end{aligned} \tag{19}$$

The $\hat{\mathbf{A}}_{\text{int}}^{(k)}$ are now given as

$$\hat{\mathbf{A}}_{\text{int}}^{(k)} = \begin{bmatrix} -\mathbf{1} - \Delta\,I_{00}\mathbf{A}_0 & \mathbf{1} - \Delta\,I_{01}\mathbf{A}_1 & \dots & -\Delta\,I_{0,N_k-1}\mathbf{A}_{N_k-1} & \mathbf{0} \\ -\mathbf{1} - \Delta\,I_{10}\mathbf{A}_0 & -\Delta\,I_{11}\mathbf{A}_1 & \dots & -\Delta\,I_{1,N_k-1}\mathbf{A}_{N_k-1} & \mathbf{0} \\ \vdots & \vdots & \ddots & \vdots & \vdots \\ -\mathbf{1} - \Delta\,I_{N_k-1,0}\mathbf{A}_0 & -\Delta\,I_{N_k-1,1}\mathbf{A}_1 & \dots & -\Delta\,I_{N_k-1,N_k-1}\mathbf{A}_{N_k-1} & \mathbf{1} \end{bmatrix} \tag{20}$$

$\hat{\mathbf{B}}_{\text{int}}^{(k)}$ and $\hat{\mathbf{q}}_{\text{int}}^{(k)}$ can be calculated in a similar way.
As the initial $\mathbf{x}_0^{(1)}$ and final $\mathbf{x}_{N_K}^{(K)}$ states are included in the optimization, initial and final boundary conditions can be imposed as simple equality constraints.

2. Adaptive Flipped Radau Pseudospectral Method

In the FRPM, the collocation points are defined on the interval $(-1, 1]$, i.e. the initial node of each segment is not collocated. Given the standard LGR points $\theta \in [-1, 1)$, the flipped values $\tilde{\theta} \in (-1, 1]$ can be computed using

$$\tilde{\theta} = \text{sort}(-\theta) \tag{21}$$

where *sort* sorts the values in ascending order. Consequently, the initial control is not part of the optimization process. In contrast to RPM, we do not include the initial node in the state approximation this time. Rather, we make use of the fact that $\mathbf{x}_0^{(1)}$ is equal to the initial boundary condition $\mathbf{x}_0$. The dynamics in differential form then read

$$D_{i0}^{(k)}\mathbf{x}_0^{(k)} + \sum_{j=1}^{N_k} D_{ij}^{(k)}\mathbf{x}_j^{(k)} = \frac{t_{N_k}^{(k)} - t_0^{(k)}}{2}\left[\mathbf{A}(\bar{\mathbf{x}}_\mathbf{i}^{(\mathbf{k})})\mathbf{x}_i^{(k)} + \mathbf{B}(\bar{\mathbf{x}}_\mathbf{i}^{(\mathbf{k})})\mathbf{u}_i^{(k)} + \mathbf{q}(\bar{\mathbf{x}}_i^{(k)}) + \boldsymbol{\nu}_i^{(k)}\right] \qquad i = 1, ..., N_k \tag{22}$$

where $\mathbf{x}_0^{(k)}$ is the initial state of each segment, and $\mathbf{x}_0^{(1)} = \mathbf{x}_0$. The integral form is

$$\mathbf{x}_i^{(k)} = \mathbf{x}_0^{(k)} + \frac{t_{N_k}^{(k)} - t_0^{(k)}}{2}\sum_{j=1}^{N_k} I_{ij}^{(k)}\left[\mathbf{A}(\bar{\mathbf{x}}_j^{(k)})\mathbf{x}_j^{(k)} + \mathbf{B}\mathbf{u}_j^{(k)} + \mathbf{q}(\bar{\mathbf{x}}_j^{(k)}) + \boldsymbol{\nu}_j^{(k)}\right] \qquad i = 1, ..., N_k \tag{23}$$

The dynamics can again be formulated as a single constraint; see [12, 35] for details.
Note that we implicitly impose the initial boundary condition by including $\mathbf{x}_0$ in Eqs. (22) and (23). Hence, only a linear equality constraint for the final boundary conditions is to be added.

B. Arbitrary-Order Legendre–Gauss–Lobatto Method

The arbitrary-order Legendre–Gauss–Lobatto discretization method relies on Hermite interpolation [37]. The idea is to use the information of the states and the dynamics at the nodal points and express the constraints at the collocation points by approximating the state variables with arbitrary-order polynomials [37, 38]. The total time of flight is divided into K segments. Each segment $[t_k, t_{k+1}]$ is mapped into the interval $[-1, 1]$ through the transformation

$$t \;\longrightarrow\; \frac{h}{2}\xi + \frac{t_{k+1} + t_k}{2} \tag{24}$$

where $\xi \in [-1, 1]$ and $h = t_{k+1} - t_k$ is the time step. In this work, nodes and collocation points are defined inside the interval $[-1, 1]$ as the roots of the derivative of the $(n-1)$th order Legendre polynomial [38], where n is the order of the method. Given n, the state $\mathbf{x}^{(k)}(\xi) \in \mathbb{R}^{n_x \times 1}$ ($n_x = 7$) is approximated inside the kth segment as

$$\mathbf{x}^{(k)}(\xi) \approx \mathbf{a}_0^{(k)} + \mathbf{a}_1^{(k)}\xi + \cdots + \mathbf{a}_n^{(k)}\xi^n, \quad k = 1, \ldots, K \tag{25}$$

where the column vectors of coefficients $\mathbf{a}_m^{(k)} \in \mathbb{R}^{n_x \times 1}$, $m = 0, \ldots, n$ are unknowns that are found by solving the following linear system:

$$\underbrace{\begin{bmatrix} \mathbf{1}_{n_x} & \theta_1\mathbf{1}_{n_x} & \theta_1^2\mathbf{1}_{n_x} & \cdots & \theta_1^n\mathbf{1}_{n_x} \\ \mathbf{1}_{n_x} & \theta_2\mathbf{1}_{n_x} & \theta_2^2\mathbf{1}_{n_x} & \cdots & \theta_2^n\mathbf{1}_{n_x} \\ \vdots & \vdots & \vdots & \vdots & \vdots \\ \mathbf{1}_{n_x} & \theta_{n_p}\mathbf{1}_{n_x} & \theta_{n_p}^2\mathbf{1}_{n_x} & \cdots & \theta_{n_p}^n\mathbf{1}_{n_x} \\ \mathbf{0}_{n_x} & \mathbf{1}_{n_x} & 2\theta_1\mathbf{1}_{n_x} & \cdots & n\theta_1^{n-1}\mathbf{1}_{n_x} \\ \vdots & \vdots & \vdots & \vdots & \vdots \\ \mathbf{0}_{n_x} & \mathbf{1}_{n_x} & 2\theta_{n_p}\mathbf{1}_{n_x} & \cdots & n\theta_{n_p}^{n-1}\mathbf{1}_{n_x} \end{bmatrix}}_{\boldsymbol{\theta}} \underbrace{\begin{bmatrix} \mathbf{a}_0^{(k)} \\ \mathbf{a}_1^{(k)} \\ \vdots \\ \mathbf{a}_{n_p}^{(k)} \\ \vdots \\ \mathbf{a}_{n-1}^{(k)} \\ \mathbf{a}_n^{(k)} \end{bmatrix}}_{\mathbf{a}^{(k)}} = \underbrace{\begin{bmatrix} \mathbf{x}^{(k)}(\theta_1) \\ \mathbf{x}^{(k)}(\theta_2) \\ \vdots \\ \mathbf{x}^{(k)}(\theta_{n_p}) \\ \frac{h}{2}\mathbf{f}_l^{(k)}(\theta_1) \\ \vdots \\ \frac{h}{2}\mathbf{f}_l^{(k)}(\theta_{n_p}) \end{bmatrix}}_{\mathbf{b}^{(k)}} \tag{26}$$

In Eq. (26), θ_j are the positions of the nodal points, $n_p = (n+1)/2$ is the number of nodes in each segment, $\mathbf{1}_{n_x}$ is the $n_x \times n_x$ identity matrix, $\mathbf{0}_{n_x}$ the $n_x \times n_x$ null matrix, and $\mathbf{f}_l(\theta_j)$ the linearized dynamics. Once the coefficients $\mathbf{a}_m^{(k)}$ have been determined as $\mathbf{a}^{(k)} = \boldsymbol{\theta}^{-1}\mathbf{b}^{(k)}$, Eq. (25) can be used to define the state and its derivative at the collocation points:

$$\begin{aligned}
\mathbf{x}^{(k)}(\zeta) &= \underbrace{\begin{bmatrix} \mathbf{1}_{n_x} & \zeta_1\mathbf{1}_{n_x} & \dots & \zeta_1^n\mathbf{1}_{n_x} \\ \mathbf{1}_{n_x} & \zeta_2\mathbf{1}_{n_x} & \dots & \zeta_2^n\mathbf{1}_{n_x} \\ \vdots & \vdots & \vdots & \vdots \\ \mathbf{1}_{n_x} & \zeta_{n_c}\mathbf{1}_{n_x} & \dots & \zeta_{n_c}^n\mathbf{1}_{n_x} \end{bmatrix}}_{\boldsymbol{\zeta}} \underbrace{\begin{bmatrix} \mathbf{a}_0^{(k)} \\ \mathbf{a}_1^{(k)} \\ \vdots \\ \mathbf{a}_n^{(k)} \end{bmatrix}}_{\mathbf{a}^{(k)}} = \boldsymbol{\zeta}\boldsymbol{\theta}^{-1}\mathbf{b}^{(k)} = \boldsymbol{\phi}\mathbf{b}^{(k)} \\
\frac{\mathrm{d}\mathbf{x}^{(k)}(\zeta)}{\mathrm{d}\xi} &= \underbrace{\begin{bmatrix} \mathbf{0}_{n_x} & \mathbf{1}_{n_x} & \dots & n\zeta_1^{n-1}\mathbf{1}_{n_x} \\ \mathbf{0}_{n_x} & \mathbf{1}_{n_x} & \dots & n\zeta_2^{n-1}\mathbf{1}_{n_x} \\ \vdots & \vdots & \vdots & \vdots \\ \mathbf{0}_{n_x} & \mathbf{1}_{n_x} & \dots & n\zeta_{n_c}^{n-1}\mathbf{1}_{n_x} \end{bmatrix}}_{\boldsymbol{\zeta}'} \underbrace{\begin{bmatrix} \mathbf{a}_0^{(k)} \\ \mathbf{a}_1^{(k)} \\ \vdots \\ \mathbf{a}_n^{(k)} \end{bmatrix}}_{\mathbf{a}^{(k)}} = \boldsymbol{\zeta}'\boldsymbol{\theta}^{-1}\mathbf{b}^{(k)} = \boldsymbol{\phi}'\mathbf{b}^{(k)}
\end{aligned} \tag{27}$$

where ζ_j are the positions of the collocation points, and $n_c = (n-1)/2$ is the number of collocation points within each segment. Similarly, the control $\mathbf{u}^{(k)}(\xi) \in \mathbb{R}^{n_u \times 1}$ ($n_u = 4$) is approximated in each segment as

$$\mathbf{u}^{(k)}(\xi) \approx \mathbf{a}_{u,0}^{(k)} + \mathbf{a}_{u,1}^{(k)}\xi + \dots + \mathbf{a}_{u,n}^{(k)}\xi^{n_p-1}, \quad k = 1,\dots,K \tag{28}$$

where the column vectors of coefficients $\mathbf{a}_{u,m}^{(k)} \in \mathbb{R}^{n_u\times 1}$, $m = 0,\dots,n$ are unknowns, obtained in a similar fashion as for the coefficients $\mathbf{a}_m^{(k)}$ inside Eq. (26). Note, however, that for the control no information about its dynamics is available and thus only the first n_p rows of the system can be considered. For this reason, the control is approximated by means of a polynomial of order $n_p - 1$. The quantities $\boldsymbol{\phi}_u$ and $\mathbf{b}_u^{(k)}$ are defined accordingly. Once the matrices and vectors corresponding to all the trajectory segments are constructed, the dynamical constraints can be written as

$$\boldsymbol{\Delta} = \boldsymbol{\Phi}'\hat{\mathbf{b}} - \frac{h}{2}[\hat{\mathbf{f}}_f + \hat{\mathbf{A}}(\boldsymbol{\Phi}\hat{\mathbf{b}} - \boldsymbol{\Phi}\hat{\mathbf{b}}^*)] + \hat{\mathbf{B}}\boldsymbol{\Phi}_u\hat{\mathbf{b}}_u = \mathbf{0} \tag{29}$$

where the capital letters and $\hat{(\cdot)}$ indicate the assembled quantities. For a detailed explanation of the method, the interested reader is referred to [13].

C. First-Order-Hold Method

Given N nodes, the time horizon is divided into $N-1$ equidistant segments with

$$t_0 = t_1 < t_2 < \dots < t_N = t_f \tag{30}$$

The control history $\mathbf{u}(t)$ is approximated as a piecewise affine function using

$$\mathbf{u}(t) = \underbrace{\frac{t_{k+1}-t}{t_{k+1}-t_k}}_{=:\lambda_-(t)}\mathbf{u}_k + \underbrace{\frac{t-t_k}{t_{k+1}-t_k}}_{=:\lambda_+(t)}\mathbf{u}_{k+1} = \lambda_-(t)\,\mathbf{u}_k + \lambda_+(t)\,\mathbf{u}_{k+1}, \qquad t \in [t_k, t_{k+1}] \tag{31}$$

where $\mathbf{u}_k$ denotes the discretized control at node k, $k = 1,\dots,N-1$. The linearized dynamics are then

$$\dot{\mathbf{x}}(t) = \mathbf{A}(t)\,\mathbf{x}(t) + \mathbf{B}\,\lambda_-(t)\,\mathbf{u}_k + \mathbf{B}\,\lambda_+(t)\,\mathbf{u}_{k+1} + \mathbf{q}(t) \tag{32}$$

Given the state transition matrix $\boldsymbol{\Phi}$ that satisfies

$$\frac{\mathrm{d}}{\mathrm{d}t}\boldsymbol{\Phi}(t,t_0) = \mathbf{A}(t)\,\boldsymbol{\Phi}(t,t_0), \qquad \boldsymbol{\Phi}(t_0,t_0) = \mathbf{1} \tag{33}$$

Eq. (32) can be rewritten in discretized form to obtain [39]

$$\mathbf{x}_{k+1} = \mathbf{A}_k\,\mathbf{x}_k + \mathbf{B}_k^-\,\mathbf{u}_k + \mathbf{B}_k^+\,\mathbf{u}_{k+1} + \mathbf{q}_k + \boldsymbol{\nu}_k \tag{34}$$

with

$$\mathbf{A}_k = \mathbf{\Phi}(t_{k+1}, t_k) \tag{35a}$$

$$\mathbf{B}_k^- = \mathbf{A}_k \int_{t_k}^{t_{k+1}} \mathbf{\Phi}^{-1}(t, t_k)\, \mathbf{B}(t)\, \lambda_-(t)\, \mathrm{d}t \tag{35b}$$

$$\mathbf{B}_k^+ = \mathbf{A}_k \int_{t_k}^{t_{k+1}} \mathbf{\Phi}^{-1}(t, t_k)\, \mathbf{B}(t)\, \lambda_+(t)\, \mathrm{d}t \tag{35c}$$

$$\mathbf{q}_k = \mathbf{A}_k \int_{t_k}^{t_{k+1}} \mathbf{\Phi}^{-1}(t, t_k)\, \mathbf{q}(t)\, \mathrm{d}t \tag{35d}$$

The state transition matrix in Eq. (33), the nonlinear dynamics in Eq. (10), and the integrands of Eqs. (35b)–(35d) are integrated simultaneously to compute $\mathbf{A}_k, \mathbf{B}_k^-, \mathbf{B}_k^+$, and $\mathbf{q}_k$ at each node. These matrices are then used to create a single equality constraint for the discretized dynamics.

Remark: The nonlinear dynamics are integrated using

$$\bar{\mathbf{x}}(t) = \bar{\mathbf{x}}_k + \int_{t_k}^{t} \mathbf{f}(\mathbf{x}(\xi), \mathbf{u}(\xi))\, \mathrm{d}\xi \tag{36}$$

to obtain the reference state at $t \in [t_k, t_{k+1}]$. In this work, we use an explicit fixed-step 8th-order Runge-Kutta method for numerically integrating Eq. (36).

IV. Trust-Region Methods

Trust-region methods use some kind of merit function to measure the progress in each iteration k. In this work, we define $\rho^{(k)}$ as the ratio

$$\rho^{(k)} = \frac{\text{actual cost decrease}}{\text{predicted cost decrease}} \tag{37}$$

where the actual cost decrease is calculated using the nonlinear constraints, and the predicted cost decrease is based on the linear constraint violations [28]. Depending on the value of $\rho^{(k)}$, the solution is accepted or rejected. In this work, we consider three trust-region methods:

1) Hard trust region with constant trust-region shrinking and growing rates.
2) Hard trust region with varying trust-region shrinking and growing rates.
3) Soft trust region with constant shrinking and growing rates.

The constraint in Eq. (11d) is imposed explicitly in hard trust-region methods, whereas in soft trust-region methods it is penalized in the objective function.

A. Hard Trust Region With Constant Rates

Hard trust regions with constant parameters are most often used in space trajectory optimization problems due to their simplicity [12, 29]. Defining three parameters $0 < \rho_0 < \rho_1 < \rho_2 < 1$, a step at iteration k is rejected if $\rho^{(k)} < \rho_0$ because this indicates that there is no (sufficiently large) progress. When a solution is accepted, the trust-region radius R is updated as follows:

$$R^{(k+1)} = \begin{cases} R^{(k)}/\alpha & \text{if} \quad \rho_0 \le \rho^{(k)} < \rho_1 \\ R^{(k)} & \text{if} \quad \rho_1 \le \rho^{(k)} < \rho_2 \\ \beta\, R^{(k)} & \text{if} \quad \rho^{(k)} \ge \rho_2 \end{cases} \tag{38}$$

where the trust-region shrinking rate $\alpha > 1$ and growing rate $\beta > 1$ are two constants.

B. Hard Trust Region With Varying Rates

We allow α and β to vary based on the values of ρ in the current k and previous iteration $k - 1$. Defining the constant parameter $\delta > 1$, α and β are updated as follows [13]:

1) If $\rho^{(k)} \geq \rho_0$ and $\rho^{(k-1)} \geq \rho_0$, then $\beta^{(k)} = \delta\beta^{(k-1)}$ and $\alpha^{(k)} = \alpha^{(k-1)}/\delta$. The growing rate is increased and the shrinking rate decreased if the previous and current iterations are accepted.
2) If $\rho^{(k)} \geq \rho_0$ and $\rho^{(k-1)} < \rho_0$, then $\beta^{(k)} = \beta^{(k-1)}/\delta$ and $\alpha^{(k)} = \delta\alpha^{(k-1)}$. The growing rate is decreased and the shrinking rate increased if only the current step is accepted.
3) If $\rho^{(k)} < \rho_0$ and $\rho^{(k-1)} \geq \rho_0$, then $\alpha^{(k)} = \alpha^{(k-1)}$ and $\beta^{(k)} = \beta^{(k-1)}$. The rates remain constant if the previous step was accepted and the current one is rejected.
4) If $\rho^{(k)} < \rho_0$ and $\rho^{(k-1)} < \rho_0$, then $\alpha^{(k)} = \delta\alpha^{(k-1)}$. The shrinking rate is increased if both steps are rejected.

In addition, bounds are imposed on α and β such that $\alpha_{\min} \leq \alpha \leq \alpha_{\max}$ and $\beta_{\min} \leq \beta \leq \beta_{\max}$.

C. Soft Trust Region

Instead of imposing the trust-region constraint in Eq. (11d) directly, we augment the performance index in Eq. (11a) with a penalty function $p(\mathbf{x})$:

$$\underset{\mathbf{u}(t)}{\text{minimize}} \qquad -z(t_f) + \lambda \, \|\boldsymbol{\nu}(t)\|_1 + \lambda \, \max(0, \eta(t)) + p(\mathbf{x}) \tag{39}$$

where $p(\mathbf{x})$ penalizes any violation of the trust-region constraint $g_{\text{TR}} \coloneqq \|\mathbf{x}(t) - \bar{\mathbf{x}}(t)\|_1 - R \leq 0$. In particular, we choose the differentiable and nondecreasing function

$$p(\mathbf{x}) = \lambda_{\text{TR}} \, \left[\max\left(0, \|\mathbf{x}(t) - \bar{\mathbf{x}}(t)\|_1 - R\right)\right]^2 \tag{40}$$

with the penalty parameter $\lambda_{\text{TR}} > 0$. The update mechanism is as follows [40]:

Case 1: $g_{\text{TR}} > 0$: reject step and set $\lambda_{\text{TR}}^{(k+1)} = \zeta \, \lambda_{\text{TR}}^{(k)}$ for $\zeta > 0$.
Case 2: $g_{\text{TR}} \leq 0$ and $\rho^{(k)} < \rho_0$: reject the step and set $R^{(k+1)} = R^{(k)}/\alpha$.
Case 3: $g_{\text{TR}} \leq 0$ and $\rho_1 \leq \rho^{(k)} < \rho_2$: accept the step and set $R^{(k+1)} = R^{(k)}/\alpha$ and $\lambda_{\text{TR}}^{(k+1)} = \lambda_{\text{TR},0}$.
Case 4: $g_{\text{TR}} \leq 0$ and $\rho^{(k)} > \rho_2$: accept the step and set $R^{(k+1)} = \beta \, R^{(k)}$ and $\lambda_{\text{TR}}^{(k+1)} = \lambda_{\text{TR},0}$.

with some parameter $\lambda_{\text{TR},0} > 0$.

V. Numerical Simulations

We assess the performance of the discretization methods in several thousand simulations. The number of converged simulations, iterations, final mass, computational time, propagation error, and the sparsity of the matrices associated with different discretization methods are compared. All simulations are carried out in MATLAB. The computational times are measured on an Intel Core i5-6300 2.30 GHz Laptop with four cores and 8 GB of RAM. The Embedded Conic Solver (ECOS) is used to solve the second-order cone program [41]. Details about the trust-region-based SCP algorithm can be found in [42, 43]. The algorithm converges if the maximum constraint violation and the relative change of the modified final mass $z(t_f)$ are lower than thresholds ε_c and ε_ϕ, respectively. The algorithm also stops if there is no sufficient progress, that is, if the relative difference of the solution vector in two consecutive iterations is smaller than ε_x. Relevant SCP parameters are given in Table 1. Different combinations of ρ_i ($i = 0, 1, 2$), α, β, and δ for the hard, and λ_{TR}, $\lambda_{\text{TR},0}$, and ζ for the soft trust-region method were assessed in preliminary simulations. We found that the values in Table 1 perform well and are often a good compromise in terms of convergence, optimality, and number of iterations. The physical constants and scaling parameters are given in Table 2. Throughout this section, we refer to (F)RPM-D and (F)RPM-I for the differential and integral formulations of the (flipped) Radau pseudospectral method, LGL for the Legendre–Gauss–Lobatto method based on Hermite interpolation, and FOH for the first-order-hold method.

A. Overview of Simulations

For each target, all combinations of different initial guesses, number of nodes, degrees of the interpolating polynomials, and trust-region methods are considered. An overview of the performed simulations is shown in Fig. 1.

1. Targets

The following three transfers are chosen for the comparison:
1) Sun-Earth Lagrange point L_2 (SEL_2) to near-Earth asteroid 2000 SG344. This is considered a simple transfer with two revolutions only.
2) Earth to Venus. A more challenging transfer with up to four revolutions and longer time of flight.

Table 1 Parameters of the SCP algorithms.

Parameter	Value
Penalty weight λ	10.0
Initial trust region R_0	100.0
ρ_0, ρ_1, ρ_2	0.01, 0.2, 0.85
α, β	1.5, 1.5
$\alpha_{\min}, \beta_{\min}$	1.01, 1.01
$\alpha_{\max}, \beta_{\max}$	4.0, 4.0
δ	1.0, 1.2
λ_{TR}, $\lambda_{\text{TR},0}$, ζ	10^{10}, 10^7, 5.0
ε_c, ε_ϕ, ε_x	10^{-6}, 10^{-4}, 10^{-7}
Max. iterations	250

Table 2 Physical constants in all simulations.

Parameter	Value
Gravitational constant μ	1.3271244×10^{11} km^3/s^2
Gravitational acceleration g_0	9.80665×10^{-3} km/s^2
Length unit LU = AU	1.495978707×10^8 km
Velocity unit VU	$\sqrt{\mu/\text{LU}}$ km/s
Time unit TU	LU/VU s
Acceleration unit ACU	VU/TU km/s^2
Mass unit MU	m_0

3) Earth to asteroid Dionysus. A complex transfer with great changes in inclination and the semi-major axis; the time of flight is almost ten years and the number of revolutions varies between three and six.

All relevant values are given in Table 3.

Table 3 Simulation values for SEL$_2$-NEA (2000 SG344), Earth-Venus and Earth-Dionysus transfers [44–46].

Parameter	SEL$_2$ - 2000 SG344	Earth - Venus	Earth - Dionysus
$\mathbf{r}_0$, LU	$[-0.70186065, 0.70623244, -3.51115 \times 10^{-5}]^\top$	$[0.97083220, 0.23758440, -1.67106 \times 10^{-6}]^\top$	$[-0.02431767, 0.98330142, -1.51168 \times 10^{-5}]^\top$
$\mathbf{v}_0$, VU	$[-0.73296949, -0.71590485, 4.40245 \times 10^{-5}]^\top$	$[-0.25453902, 0.96865497, 1.50402 \times 10^{-5}]^\top$	$[-1.01612926, -0.02849401, 1.69550 \times 10^{-6}]^\top$
m_0, kg	22.6	1500	4000
$\mathbf{r}_f$, LU	$[0.41806795, 0.82897114, -0.00143382]^\top$	$[-0.32771780, 0.63891720, 0.02765929]^\top$	$[-2.04061782, 2.05179130, 0.55428895]^\top$
$\mathbf{v}_f$, VU	$[-0.96990332, 0.43630220, -0.00123381]^\top$	$[-1.05087702, -0.54356747, 0.05320953]^\top$	$[-0.14231932, -0.45108800, 0.01894690]^\top$
m_f, kg	free	free	free
$T_{\max}$, N	2.2519×10^{-3}	0.33	0.32
I_{sp}, s	3067	3800	3000
t_f, days	700	1000	3534

2. Initial Guess

Two different methods to generate the initial guesses are used:

1) Shape-based approach: a simple cubic interpolation based on [47] where the number of revolutions is varied between 1.6 and 2.6 (2000 SG344), 2.0 and 4.5 (Venus), and 3.0 and 6.0 (Dionysus). This results in infeasible state trajectories and in almost all cases (when the number of revolutions is not an integer) the final boundary conditions are not satisfied. The controls are set to zero.
2) Propagation: the nonlinear dynamics are propagated for t_f with tangential thrust and different thrust magnitudes ranging from 0 to $T_{\max}$.

The comparison of an optimal trajectory and the ones generated with cubic interpolation and propagation are illustrated in Fig. 2. Clearly, the optimal one deviates significantly and the final positions of the initial guesses are far from the target position.

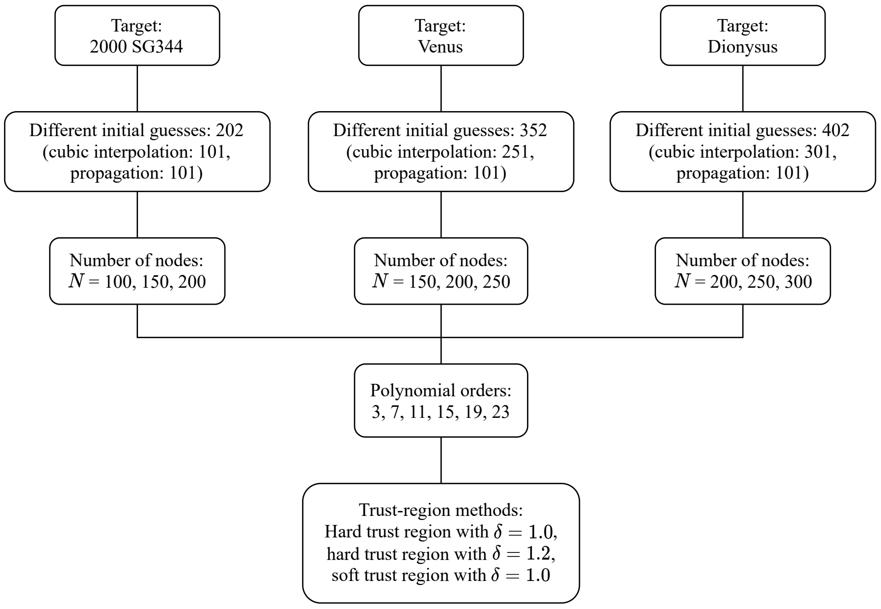
Target:
2000 SG344
Target:
Venus
Target:
Dionysus
Different initial guesses: 202
(cubic interpolation: 101,
propagation: 101)
Different initial guesses: 352
(cubic interpolation: 251,
propagation: 101)
Different initial guesses: 402
(cubic interpolation: 301,
propagation: 101)
Number of nodes:
N = 100, 150, 200
Number of nodes:
N = 150, 200, 250
Number of nodes:
N = 200, 250, 300
Polynomial orders:
3, 7, 11, 15, 19, 23
Trust-region methods:
Hard trust region with δ = 1.0,
hard trust region with δ = 1.2,
soft trust region with δ = 1.0

Fig. 1 Overview of performed simulations.

3. Polynomial Orders

For RPM, FRPM, and LGL, different orders of the interpolating polynomials for the state trajectories are considered, ranging from 3 to 23 (see Table 4). Higher orders are not suitable for onboard implementation due to the high computational effort.

4. Number of Nodes

As the times of flight and number of revolutions vary considerably, we choose three different nominal discretization points N for each transfer (see Table 4). Due to the different nature of the discretization methods, the segments are chosen such that the actual number of nodes is closest to the nominal one.

Table 4 Number of nodes and orders of the interpolating polynomials for each transfer.

Parameter	SEL$_2$ - 2000 SG344	Earth - Venus	Earth - Dionysus
Nodes	100, 150, 200	150, 200, 250	200, 250, 300
Polynomial orders		3, 7, 11, 15, 19, 23	

5. Trust-Region Methods

Two hard trust regions with $\delta = 1.0$ and $\delta = 1.2$, respectively, and a soft trust region with $\delta = 1.0$ are compared.

The total number of simulations n_{sim} for each discretization method is given in Table 5. It is determined using

$$n_{\text{sim}} = n_{\text{guess}} \cdot n_{\text{nodes}} \cdot n_{\text{TR}} \cdot n_{\text{orders}} \tag{41}$$

where n_{guess} is the total number of initial guesses obtained with the cubic-based and the propagation approaches, $n_{\text{nodes}} = 3$ the number of different nominal nodes, $n_{\text{TR}} = 3$ the number of trust-region methods, and $n_{\text{orders}} = 6$ the number of polynomial orders. Note that this term is only considered for LGL and RPM/FRPM.

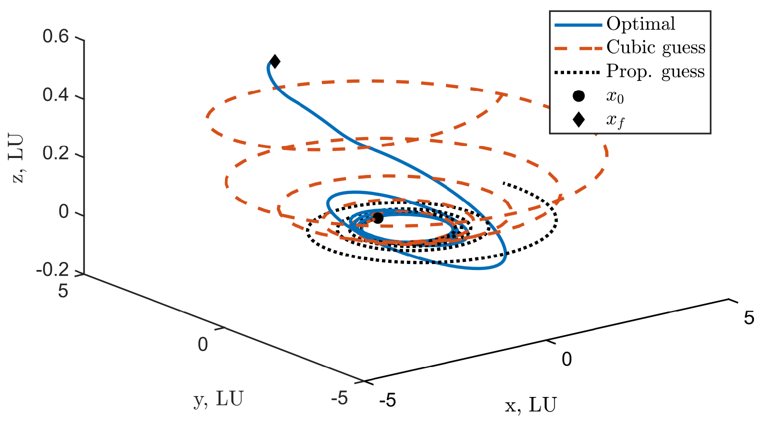

Fig. 2 Optimal trajectory and initial guesses generated with cubic interpolation and propagation with 0.5 $T_{\max}$ for a Dionysus transfer (N = 250).

Table 5 Total number of simulations for each target and each discretization method.

Target	FOH	LGL, RPM-D, RPM-I, FRPM-D, FRPM-I
2000 SG344	1818	10908
Venus	3168	19008
Dionysus	3618	21708

B. Results

1. Convergence, Iterations, and Final Mass

We assess the performance of our algorithms by means of four analyses for each of the transfers. The objective is to understand the influence of the discretization method, the order of the interpolating polynomial, the number of nodes, and the trust-region method on the success rate, the iterations required to reach convergence, and the optimality of the solutions. For this reason, for each of the aforementioned parameters, we take the median of the obtained results by varying all the other parameters. For example, the comparison of the discretization methods is performed by taking the median of all results obtained with a given method for all polynomial orders, all considered nodes, and all trust-region strategies. The outcome of the analyses is reported in Figs. 3 - 5, where the results related to asteroid 2000 SG344, Venus, and asteroid Dionysus are presented, respectively. The error bars represent the 70th percentile of the considered quantity.

With regard to asteroid 2000 SG344, the largest number of converged cases is obtained with FOH (success rate of approximately 80%); LGL yields only slightly fewer, pseudospectral methods approximately 10% fewer converged cases. The number of iterations is similar, even though FOH requires the fewest. The obtained final masses are almost the same for all methods. Notably, lower orders require fewer iterations than higher orders. The convergence increases for higher polynomial degrees up to 15, and then remains almost constant. The number of nodes seems to have a rather small influence on the results; nevertheless, the convergence is slightly higher when N is increased, and the number of iterations reduces. The hard trust-region with δ = 1.0 and the soft trust-region method yield equivalent results. As expected, the hard trust-region approach with δ = 1.2 requires only half as many iterations as with δ = 1.0 at the cost of fewer converged simulations.

Regarding Venus, the tendency of the methods is opposite: the pseudospectral methods are able to find solutions in almost 60% of the cases, therefore having a 10% higher success rate compared to FOH and LGL (see Fig. 4). Furthermore, the overall convergence is worse compared to 2000 SG344. The number of iterations and final masses are similar. Even though the convergence also improves for higher orders, the difference is less significant. The number of nodes and the trust-region method seem to have a small impact on the results (except for the fewer number of iterations

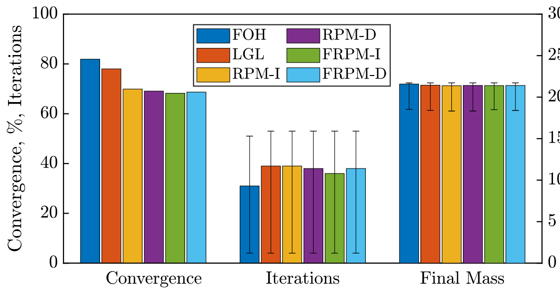

(a) Comparison of discretization methods.

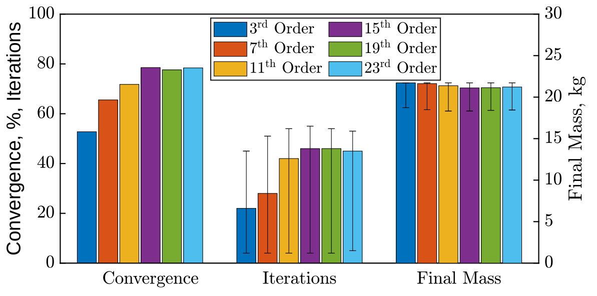

(b) Comparison of the orders of the interpolating polynomial.

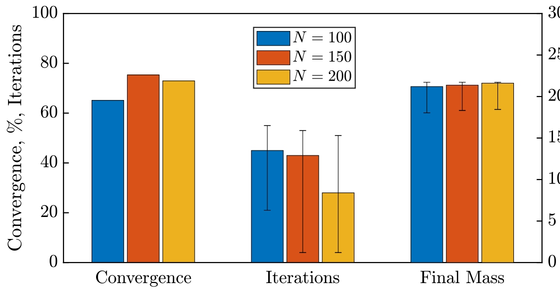

(c) Comparison of the number of nodes.

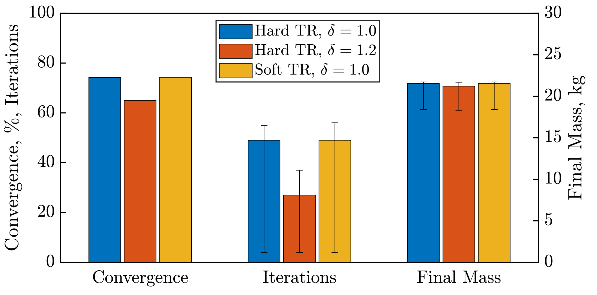

(d) Comparison of trust-region methods.

Fig. 3 Influence of the discretization method, the order of the interpolating polynomial, the number of nodes, and the trust-region method on convergence, iterations, and final mass for the transfer to asteroid 2000 SG344.

when choosing $\delta = 1.2$).

In the Dionysus case, FOH and LGL yield 10% more converged simulations than the pseudospectral methods (see Fig. 5). Remarkably, the behavior of the polynomial orders is opposite in this case: apart from the third order that yields the lowest success rate, the convergence is best for the 7th order and decreases as the order increases. The influence of the number of nodes is again small, and the trust-region methods show the same behavior as in the previous cases.

As the previous plots considered all orders, Fig. 6 shows the convergence for all targets for the most relevant polynomial degrees 7 and 11. This way the potentially poor performance of the third order does not bias the results. Apparently, the bars follow the same trend: FOH and LGL seem to outperform the pseudospectral methods for the transfers to the asteroids 2000 SG344 and Dionysus. With regard to Venus, in contrast, RPM and FRPM achieve higher success rates.

Figure 7 shows the convergence for the cubic interpolation and propagation guesses. Due to the similarity of the initial and final orbits, the success rate of approximately 70% for the transfer to asteroid 2000 SG344 is high regardless of how the initial guess is generated. With regard to Venus and Dionysus, however, propagating with tangential thrust results in poor guesses that deviate considerably from the optimal trajectories. A success rate of almost 50% is therefore remarkable. Still, using a cubic interpolation guess yields in general a larger number of converged cases.

2. Accuracy

Apart from convergence, it is crucial that a discretization method is able to achieve a certain accuracy. We define the propagation error for the position as $\left\|\mathbf{r}(t_f)_{\text{prop}} - \mathbf{r}(t_f)\right\|_2$ where $\mathbf{r}(t_f)_{\text{prop}}$ is the final position that is obtained by integrating the dynamics with the optimized controls (the error for the velocity is defined accordingly). As the thrust profile is only known at the discretization points, the controls need to be interpolated for the integration using Eqs. (14) (28), and (31), respectively. Figure 8 shows the orders of magnitude of the propagation error for a Dionysus transfer. It is evident that all methods and polynomial orders achieved the desired accuracy of 10^{-6} LU except for the third order. More precisely, almost all methods found solutions with a median error of 10^{-7} LU or less; only some LGL orders failed to do so in a few cases. The propagation error for the velocity shows a similar tendency, often being one order of magnitude smaller than the position error. The same statements are true for the other targets. Although the propagation error is small for all methods, the interpolated controls violate the constraints on the thrust magnitude for LGL and RPM/FRPM as shown in Fig. 9. The reason is that polynomial interpolation results in oscillations close to the edges of

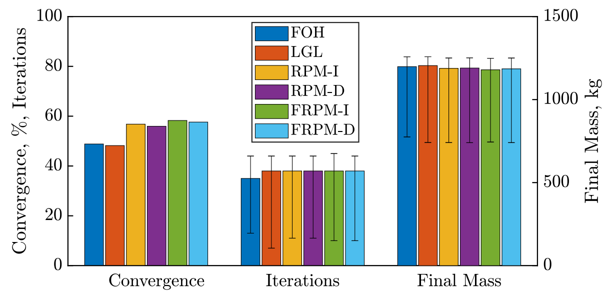

(a) Comparison of discretization methods.

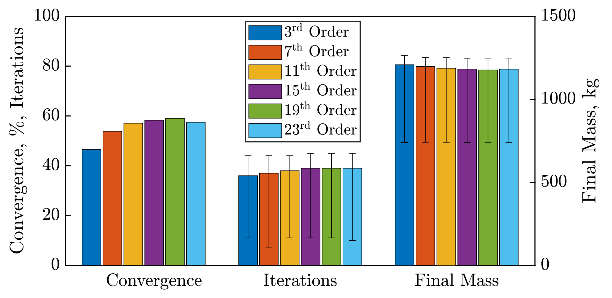

(b) Comparison of the orders of the interpolating polynomial.

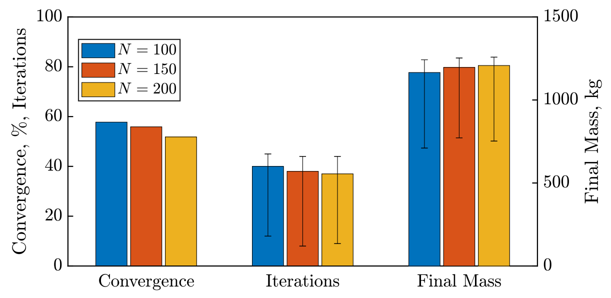

(c) Comparison of the number of nodes.

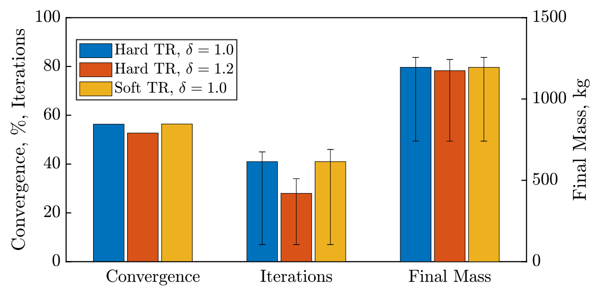

(d) Comparison of trust-region methods.

Fig. 4 Influence of the discretization method, the order of the interpolating polynomial, the number of nodes, and the trust-region method on convergence, iterations, and final mass for the transfer to Venus.

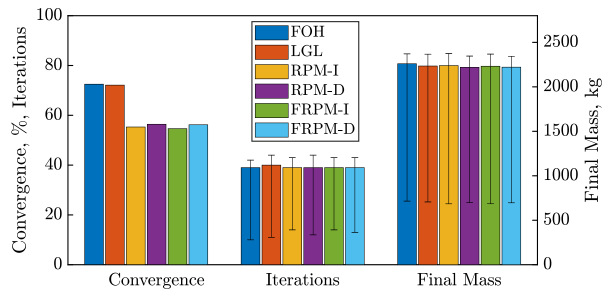

(a) Comparison of discretization methods.

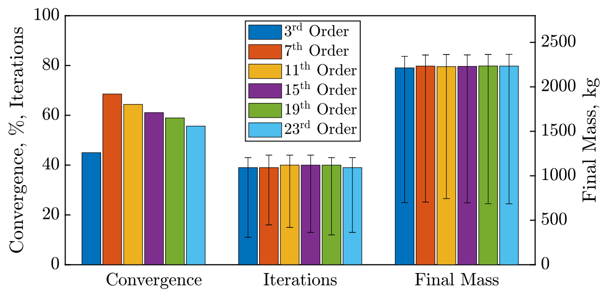

(b) Comparison of the orders of the interpolating polynomial.

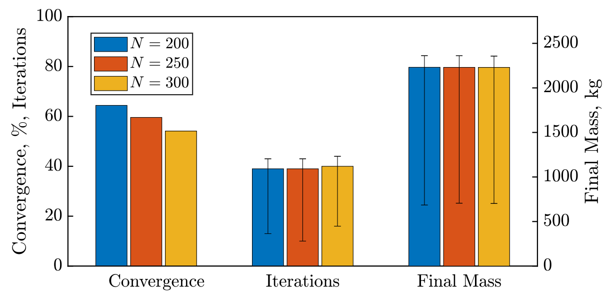

(c) Comparison of number of nodes.

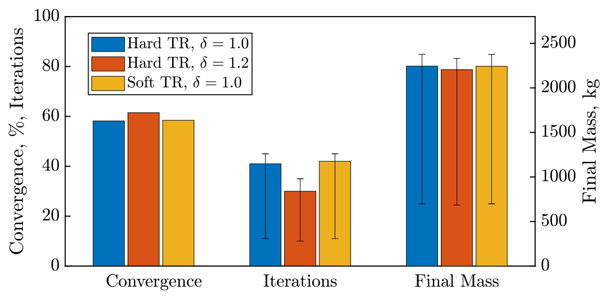

(d) Comparison of trust-region methods.

Fig. 5 Influence of the discretization method, the order of the interpolating polynomial, the number of nodes, and the trust-region method on convergence, iterations, and final mass for the transfer to Dionysus.

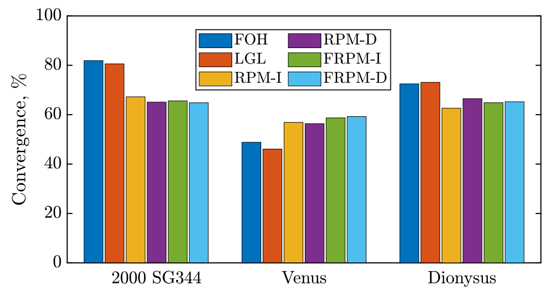

Fig. 6 Comparison of convergence for polynomial orders 7 and 11 for all targets.

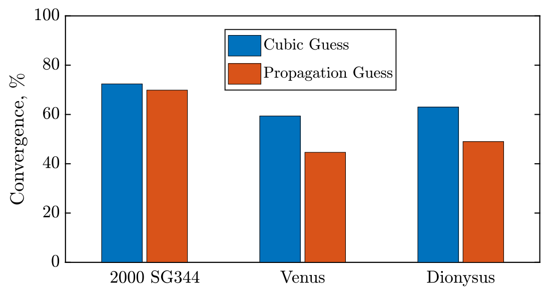

Fig. 7 Comparison of convergence for different initial guesses for all targets.

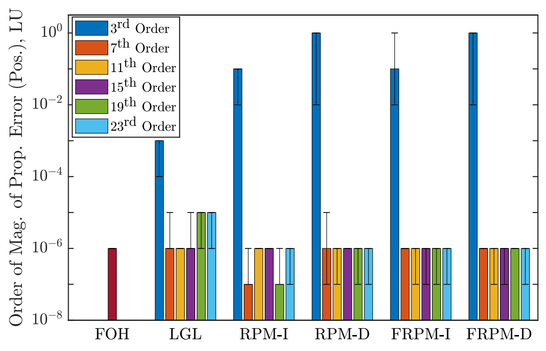

Fig. 8 Comparison of the order of magnitude of the propagation error (position) for a Dionysus transfer (N = 250). Median with minimum and maximum values is shown.

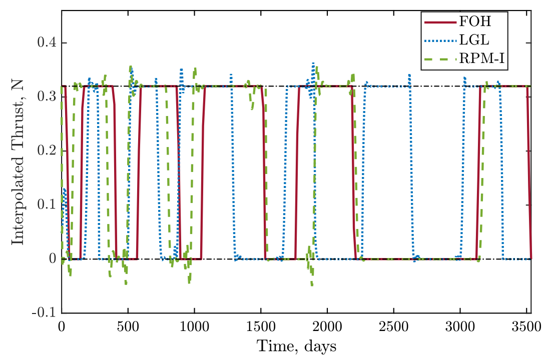

Fig. 9 Interpolated control profiles obtained with FOH and 11th order polynomials (LGL/RPM) for a Dionysus transfer (N = 250). The black dash-dotted lines represent the lower and upper bounds.

the segments for higher orders (Runge phenomenon). Only FOH is able to generate a bang-bang control profile that does not violate the bounds due to the linear interpolation.

3. Computational Time and Memory

Computational time and memory are two other important aspects to consider. As we are dealing with a large amount of optimization parameters, sparse linear algebra becomes crucial. Dense matrix operations would not only take longer to compute, but might also result in memory problems for large-scale optimization problems. The typical percentage of the nonzero elements in the linear equality constraints matrix is given in Fig. 10. Even though more than 99% of the elements are zero for all methods, the integral formulations of RPM/FRPM and LGL are several times denser than (F)RPM-D and FOH. This increases the time required to solve the SOCP, therefore resulting in a higher total CPU time when the number of iterations does not change. Figure 11a shows the computational times per SCP iteration for a typical Dionysus transfer. As expected, the computational effort increases for higher orders as the matrices become denser. Remarkably, for the four pseudospectral methods the solver time accounts for the largest portion of the total time, whereas for FOH and LGL the time outside the solver is larger. This is because of the integration (FOH) and the transformations due to the definition of the nodes and collocation points (LGL). Moreover, LGL requires the greatest computational effort among all methods regardless of the transfer (see Fig. 11b where the most relevant orders 7 and 11 are shown). The difference becomes more significant when the number of nodes is increased. In general, pseudospectral methods with orders 7 and 11 seem to be the fastest, directly followed by FOH which eventually outperforms all other methods when higher orders are considered. Given the typical number of iterations of 40, the maximum total CPU time is approximately 24 seconds for FOH and (F)RPM, and 52 seconds for LGL. Although the integral formulations of (F)RPM are denser, their CPU times are sometimes lower than the ones obtained with (F)RPM-D due to the smaller number of solver iterations.

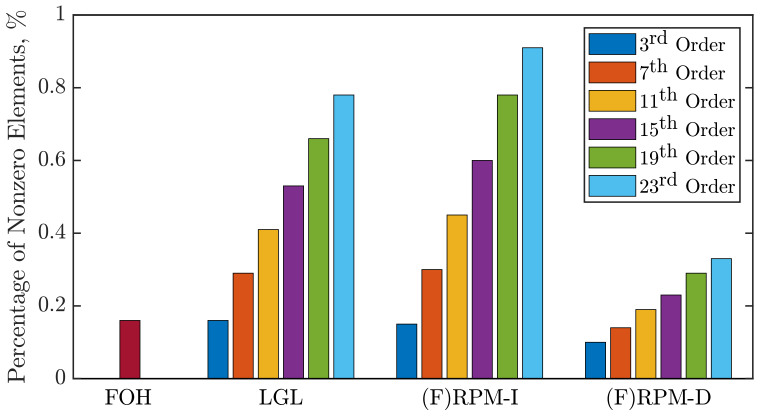

Fig. 10 Comparison of the number of nonzero elements of the linear equality constraints matrix for a Dionysus transfer (N = 250).

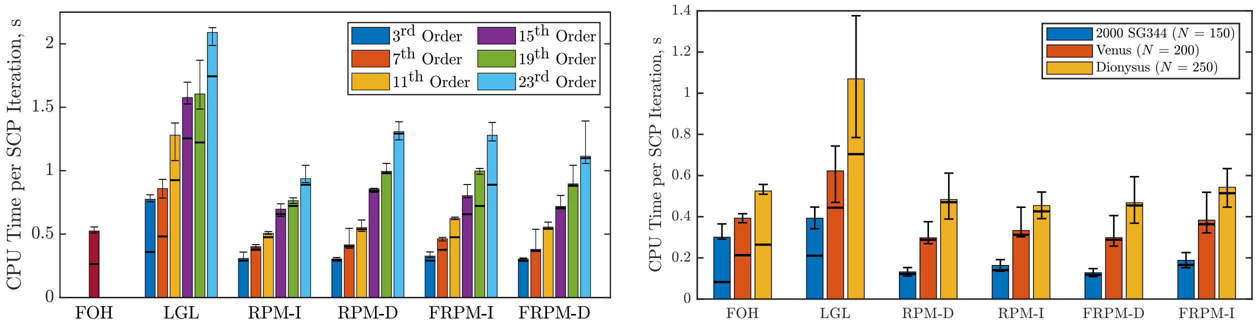

(a) CPU times for different polynomial orders for a Dionysus transfer (N = 250).

(b) Mean CPU times for polynomial orders 7 and 11 for all targets.

Fig. 11 Comparison of CPU times per SCP iteration obtained with the hard trust-region method and δ = 1.0. Median with minimum and maximum values is shown. The heights of the bars show the total CPU times, the horizontal lines within each bar indicate the times required to solve one SOCP.

C. Discussion

We briefly summarize and discuss the results of the simulations:

1) All methods achieve a high percentage of converged cases despite the large perturbations. Yet, approximations with third-order polynomials often fail to obtain a feasible solution for more complex problems.
2) All trust-region methods yield similar results. Due to the chosen weights, the soft trust-region is equivalent to the hard trust-region method, but requires more iterations to solve each second-order cone program (SOCP), and hence more computational time.
3) The hard trust-region method with δ = 1.2 often finds fewer feasible solutions, but requires considerably fewer iterations and therefore lower CPU times.
4) Except for a few cases, the influence of the number of nodes on the convergence and number of iterations is often small. Yet, even though not relevant for the number of nodes that we have chosen, a too small N might result in a larger propagation error.
5) The number of nodes, polynomial order, discretization and trust-region methods have a negligible effect on the final mass.
6) Pseudospectral methods seem to yield similar results regardless of the transfer, whereas FOH and LGL often obtain different success rates for different transfers. FOH and LGL behave similarly in all simulations.
7) The propagation errors are low for all methods. Only third-order polynomials cannot achieve the required accuracy for longer flight times and more revolutions. There is no significant improvement in the accuracy when using polynomials with orders greater than 7 or 11.

8) Control interpolation results in oscillations for LGL and RPM/FRPM, therefore violating the bounds on the thrust magnitude. Only FOH yields an accurate bang-bang thrust profile.
9) All methods yield very sparse matrices. Especially FOH and the differential formulations of RPM and FRPM result in the smallest number of nonzero elements; often only few hundreds of kilobytes of memory are required.
10) The computational time increases for higher orders as the matrices become denser. Typical computational times are 0.2 - 0.6 seconds per SCP iteration (FOH and 7th - 11th order RPM/FRPM) and 0.4 - 1.3 seconds (LGL). Given 40 iterations at most, obtaining a solution requires maximum 24 seconds (FOH and RPM/FRPM) and 52 seconds (LGL).
11) FOH and RPM/FRPM yield lower CPU times than LGL in all simulations. For FOH and LGL with lower orders, the SOCP solution time is similar to the time outside the solver. This is due to the integration (FOH) and transformations (LGL), respectively.

There are several requirements for onboard guidance methods. We briefly assess the discretization methods in terms of reliability and robustness, onboard capability, accuracy, and optimality, and give a final recommendation.

Reliability and robustness. All methods are robust against poor initial guesses and achieve a high success rate. This is crucial for onboard applications as the algorithm must not fail. As previous optimal trajectories can be reused in an autonomous guidance scenario, the initial guesses are no longer poor and therefore, the convergence is expected to be close to 100% (see also [34, 35]). All trust-region methods are reliable.

Onboard capability. The discretization method must be compatible with the limited hardware onboard. The obtained CPU times would result in a total computational time of few minutes for typical space-flight processors such as the LEON family (see e.g. [43] and [48]), therefore being acceptable for deep-space cruise which can last several years. FOH and RPM/FRPM with orders 7 - 11 are preferable due to the lower CPU times. Note that the real solving times are lower when considering previous optimal trajectories. Using a compiled language like C or C++ will also decrease the computational time. Given the high sparsity of the parameter optimization problem, often only few hundreds of kilobytes of memory are required; this seems acceptable for current processors. Hard trust regions are preferable due to the lower computational effort.

Accuracy. All methods achieve the desired high accuracy which is needed to eventually reach the target. However, interpolating the controls results in oscillations for LGL and RPM/FRPM. This behavior is not desirable as it violates the bounds on the thrust magnitude and does not represent the true bang-bang thrust profile. The linear control interpolation in FOH seems therefore more suitable for fuel-optimal problems. Moreover, in real missions, it is often desirable to have only few changes in the control profile within each trajectory segment. A low-order approximation of the controls as in FOH is therefore preferable.

Optimality. As the propellant mass is limited, optimal solutions are sought. All discretization and trust-region methods fulfil this criterion as they yield similar final masses that are close to the optimal ones found in literature.

We therefore consider FOH as the most suitable method for onboard low-thrust fuel-optimal trajectory optimization in deep space. A hard trust-region method is preferable, and often $\delta = 1.2$ appears to be a good compromise.

VI. Conclusion

This paper assesses the discretization methods first-order hold, an arbitrary-order Legendre–Gauss–Lobatto method with Hermite interpolation, and different formulations of the Radau pseudospectral method for the low-thrust trajectory optimization problem. The influence of the discretization method, order of the interpolating polynomial, number of nodes, and trust-region strategy are investigated.

Although orders between 7 and 11 for the collocation methods seem to be suitable for onboard applications, FOH yields the best compromise in terms of convergence, onboard capability, accuracy, and optimality. Even though this work does not present a convergence proof, the high percentage of converged cases has shown that SCP is very reliable despite the poor initial guesses. This is crucial for real-time guidance as a solution must be obtained at any time. Similar to powered descent landing guidance, our results show that a convex programming approach seems to be a viable method to compute low-thrust trajectories onboard.

Acknowledgments

This research is part of EXTREMA, a project that has received funding from the European Research Council (ERC) under the European Union's Horizon 2020 research and innovation programme (Grant Agreement No. 864697).

References

[1] Klesh, A., and Krajewski, J., "MarCO: Mars Cube One – Lessons Learned from Readying the First Interplanetary Cubesats for Flight," *49th Lunar and Planetary Science Conference*, 2018.

[2] Tsiotras, P., and Mesbahi, M., "Toward an Algorithmic Control Theory," *Journal of Guidance, Control, and Dynamics*, Vol. 40, No. 2, 2017, pp. 194–196. https://doi.org/10.2514/1.G002754.

[3] Lu, P., "Introducing Computational Guidance and Control," *Journal of Guidance, Control, and Dynamics*, Vol. 40, No. 2, 2017, pp. 193–193. https://doi.org/10.2514/1.G002745.

[4] Açıkmeşe, B., Aung, M., Casoliva, J., Mohan, S., Johnson, A., Scharf, D., Masten, Scotkin, D., Wolf, A., , and Regehr, M., "Flight Testing of Trajectories Computed by G-FOLD: Fuel Optimal Large Divert Guidance Algorithm for Planetary Landing," *AAS/AIAA Space Flight Mechanics Meeting*, Kauai, HI, USA, 2013. AAS Paper 13-386.

[5] Reynolds, T., Malyuta, D., Mesbahi, M., Açıkmeşe, B., and Carson, J. M., "A Real-Time Algorithm for Non-Convex Powered Descent Guidance," *AIAA Scitech 2020 Forum*, 2020. https://doi.org/10.2514/6.2020-0844.

[6] Betts, J. T., "Survey of Numerical Methods for Trajectory Optimization," *Journal of Guidance, Control, and Dynamics*, Vol. 21, No. 2, 1998, pp. 193 – 207. https://doi.org/10.2514/2.4231.

[7] Conway, B. A., "A Survey of Methods Available for the Numerical Optimization of Continuous Dynamic Systems," *Journal of Optimization Theory and Applications*, Vol. 152, No. 2, 2012, pp. 271 – 306. https://doi.org/10.1007/s10957-011-9918-z.

[8] Mao, Y., Szmuk, M., and Açıkmeşe, B., "A Tutorial on Real-time Convex Optimization Based Guidance and Control for Aerospace Applications," *2018 Annual American Control Conference (ACC)*, 2018, pp. 2410–2416. https://doi.org/10.23919/ACC.2018.8430984.

[9] Dueri, D., Açıkmeşe, B., Scharf, D. P., and Harris, M. W., "Customized Real-Time Interior-Point Methods for Onboard Powered-Descent Guidance," *Journal of Guidance, Control, and Dynamics*, Vol. 40, No. 2, 2017, pp. 197–212. https://doi.org/10.2514/1.G001480.

[10] Reynolds, T. P., and et al., "SOC-i: A CubeSat Demonstration of Optimization-Based Real-Time Constrained Attitude Control," *IEEE Aerospace Conference*, virtual, 2020.

[11] Açıkmeşe, B., and Ploen, S. R., "Convex Programming Approach to Powered Descent Guidance for Mars Landing," *Journal of Guidance, Control, and Dynamics*, Vol. 30, No. 5, 2007, pp. 1353–1366. https://doi.org/10.2514/1.27553.

[12] Hofmann, C., and Topputo, F., "Rapid Low-Thrust Trajectory Optimization in Deep Space Based On Convex Programming," *Journal of Guidance, Control, and Dynamics*, Vol. 44, No. 7, 2021, pp. 1379–1388. https://doi.org/10.2514/1.G005839.

[13] Morelli, A. C., Hofmann, C., and Topputo, F., "Robust Low-Thrust Trajectory Optimization Using Convex Programming and a Homotopic Approach," *IEEE Transactions on Aerospace and Electronic Systems*, 2021. https://doi.org/10.1109/TAES.2021.3128869, available online.

[14] Wang, Z., and Grant, M. J., "Minimum-Fuel Low-Thrust Transfers for Spacecraft: A Convex Approach," *IEEE Transactions on Aerospace and Electronic Systems*, Vol. 54, No. 5, 2018, pp. 2274–2290. https://doi.org/10.1109/TAES.2018.2812558.

[15] Wang, Z., and Lu, Y., "Improved Sequential Convex Programming Algorithms for Entry Trajectory Optimization," *Journal of Spacecraft and Rockets*, Vol. 57, No. 6, 2020, pp. 1373–1386. https://doi.org/10.2514/1.A34640.

[16] Topputo, F., and Zhang, C., "Survey of Direct Transcription for Low-Thrust Space Trajectory Optimization with Applications," *Abstract and Applied Analysis*, Vol. 2014, 2014, pp. 1–15. https://doi.org/10.1155/2014/851720.

[17] Williams, P., "Hermite–Legendre–Gauss–Lobatto Direct Transcription in Trajectory Optimization," *Journal of Guidance, Control, and Dynamics*, Vol. 32, No. 4, 2009, pp. 1392–1395. https://doi.org/10.2514/1.42731.

[18] L. Darby, W. W. Hager, A. V. R., "An hp-Adaptive Pseudospectral Method for Solving Optimal Control Problems," *Optimal Control Applications and Methods*, Vol. 32, 2010, pp. 476–502. https://doi.org/10.1002/oca.

[19] Rao, A. V., "A Survey of Numerical Methods for Trajectory Optmization," *AAS/AIAA Astrodynamics Specialist Conference*, Pittsburgh, PA, USA, 2009. AAS Paper 09-334.

[20] Benson, D. A., Huntington, G. T., Thorvaldsen, T. P., and Rao, A. V., "Direct Trajectory Optimization and Costate Estimation via an Orthogonal Collocation Method," *Journal of Guidance, Control, and Dynamics*, Vol. 29, No. 6, 2006, pp. 1435–1440. https://doi.org/10.2514/1.20478.

[21] Garg, D., Patterson, M. . A., Francolin, C., L. Darby, C. L., Huntington, G. T., Hager, W. W., and Rao, A. V., "Direct trajectory optimization and costate estimation of finite-horizon and infinite-horizon optimal control problems using a Radau pseudospectral method," *Computational Optimization and Applications*, Vol. 49, No. 2, 2011, pp. 335–358. https://doi.org/10.2514/1.20478.

[22] Sagliano, M., "Generalized hp Pseudospectral-Convex Programming for Powered Descent and Landing," *Journal of Guidance, Control, and Dynamics*, Vol. 42, No. 7, 2019. https://doi.org/10.2514/1.G003731.

[23] Yu, C., and Zhao, Y., D. Yang, "Efficient Convex Optimization of Reentry Trajectory via the Chebyshev Pseudospectral Method," *International Journal of Aerospace Engineering*, Vol. 2019, 2019. https://doi.org/10.1155/2019/1414279, article 1414279.

[24] Tang, G., Jiang, F., and Li, J., "Fuel-Optimal Low-Thrust Trajectory Optimization Using Indirect Method and Successive Convex Programming," *IEEE Transactions on Aerospace and Electronic Systems*, Vol. 54, No. 4, 2018, pp. 2053–2066. https://doi.org/10.1109/TAES.2018.2803558.

[25] Reynolds, T. P., Szmuk, M., Malyuta, D., Mesbahi, M., Açıkmeşe, B., and Carson, J. M., "Dual Quaternion-Based Powered Descent Guidance with State-Triggered Constraints," *Journal of Guidance, Control, and Dynamics*, Vol. 43, No. 9, 2020, pp. 1584–1599. https://doi.org/10.2514/1.G004536.

[26] Kayama, Y., Howell, K. C., Bando, M., and Hokamoto, S., "Low-Thrust Trajectory Design with Convex Optimization for Libration Point Orbits," *AAS/AIAA Space Flight Mechanics Meeting*, 2021. AAS Paper 21-231.

[27] Malyuta, D., Reynolds, T., Szmuk, M., Mesbahi, M., Açıkmeşe, B., and Carson, J. M., "Discretization Performance and Accuracy Analysis for the Rocket Powered Descent Guidance Problem," *AIAA Scitech 2019 Forum*, 2019. https://doi.org/10.2514/6.2019-0925.

[28] Mao, Y., Szmuk, M., Xu, X., and Açıkmeşe, B., "Successive Convexification: A Superlinearly Convergent Algorithm for Non-convex Optimal Control Problems," , Preprint, submitted February 2019. https://arxiv.org/abs/1804.06539.

[29] Wang, Z., and Grant, M. J., "Minimum-Fuel Low-Thrust Transfers for Spacecraft: A Convex Approach," *IEEE Transactions on Aerospace and Electronic Systems*, Vol. 54, No. 5, 2018, pp. 2274–2290. https://doi.org/10.1109/TAES.2018.2812558.

[30] Garg, D., Patterson, M., Hager, W., Rao, A., Benson, D., and Huntington, G., "An overview of three pseudospectral methods for the numerical solution of optimal control problems," *Advances in the Astronautical Sciences*, Vol. 135, 2009.

[31] Williams, P., "Hermite–Legendre–Gauss–Lobatto Direct Transcription in Trajectory Optimization," *Journal of Guidance, Control, and Dynamics*, Vol. 32, No. 4, 2009, pp. 1392–1395. https://doi.org/10.2514/1.42731.

[32] Garg, D., "Advances in Global Pseudospectral Methods for Optimal Control," Ph.D. thesis, University of Florida, 2011.

[33] Berrut, J.-P., and Trefethen, L. N., "Barycentric Lagrange Interpolation," *SIAM Review*, Vol. 46, No. 3, 2004. https://doi.org/10.1137/S0036144502417715.

[34] Hofmann, C., and Topputo, F., "Pseudospectral Convex Low-Thrust Trajectory Optimization in a High-Fidelity Model," *AAS/AIAA Space Flight Mechanics Meeting*, 2021. AAS Paper 21-678.

[35] Hofmann, C., and Topputo, F., "Closed-Loop Guidance for Low-Thrust Interplanetary Trajectories Using Convex Programming," *11th International ESA Conference on Guidance, Navigation & Control Systems*, 2021. Paper 46.

[36] Françolin, C. C., Benson, D. A., Hager, W. W., and Rao, A. V., "Costate approximation in optimal control using integral Gaussian quadrature orthogonal collocation methods," *Optimal Control Applications and Methods*, Vol. 36, No. 4, 2015, pp. 381–397. https://doi.org/https://doi.org/10.1002/oca.2112.

[37] Topputo, F., and Zhang, C., "Survey of Direct Transcription for Low-Thrust Space Trajectory Optimization with Applications," *Abstract and Applied Analysis*, Vol. 2014, 2014. https://doi.org/10.1155/2014/851720.

[38] Williams, P., "Hermite–Legendre–Gauss–Lobatto Direct Transcription in Trajectory Optimization," *Journal of Guidance, Navigation, and Control*, Vol. 32, No. 4, 2009, pp. 1392–1395. https://doi.org/10.2514/1.42731.

[39] Rugh, W. J., *Linear System Theory*, 2$^{\text{nd}}$ ed., Prentice-Hall, 1996.

[40] Bonalli, R., Cauligi, A., Bylard, A., and Pavone, M., "GuSTO: Guaranteed Sequential Trajectory optimization via Sequential Convex Programming," *2019 International Conference on Robotics and Automation (ICRA)*, 2019, pp. 6741–6747. https://doi.org/10.1109/ICRA.2019.8794205.

[41] Domahidi, A., Chu, E., and Boyd, S., "ECOS: An SOCP Solver for Embedded Systems," *European Control Conference*, Zurich, Switzerland, 2013, pp. 3071–3076. https://doi.org/doi:10.23919/ECC.2013.6669541.

[42] Mao, Y., Szmuk, M., Xu, X., and Açıkmeşe, B., "Successive Convexification: A Superlinearly Convergent Algorithm for Non-convex Optimal Control Problems," , Preprint, submitted February 2019. https://arxiv.org/abs/1804.06539.

[43] Hofmann, C., and Topputo, F., "Toward On-Board Guidance of Low-Thrust Spacecraft in Deep Space Using Sequential Convex Programming," *Proceedings of AAS/AIAA Space Flight Mechanics Meeting AAS Paper 21-350*, 2021, pp. 1–19.

[44] Topputo, F., Wang, Y., Giordano, G., Franzese, V., Goldberg, H., Perez-Lissi, F., and Walker, R., "Envelop of Reachable Asteroids by M-ARGO CubeSat," *Advances in Space Research*, Vol. 67, No. 12, 2021, pp. 4193–4221. https://doi.org/10.1016/j.asr.2021.02.031.

[45] Jiang, F., Baoyin, H., and Li, J., "Practical Techniques for Low-Thrust Trajectory Optimization with Homotopic Approach," *Journal of Guidance, Control, and Dynamics*, Vol. 35, No. 1, 2012. https://doi.org/10.2514/1.52476.

[46] Taheri, E., Kolmanovsky, I., and Atkins, E., "Enhanced Smoothing Technique for Indirect Optimization of Minimum-Fuel Low-Thrust Trajectories," *Journal of Guidance, Control, and Dynamics*, Vol. 39, No. 11, 2016. https://doi.org/10.2514/1.G000379.

[47] Taheri, E., and Abdelkhalik, O., "Initial Three-Dimensional Low-Thrust Trajectory Design," *Advances in Space Research*, Vol. 57, No. 3, 2016, pp. 889 – 903. https://doi.org/10.1016/j.asr.2015.11.034.

[48] Massari, M., Lizia, P. D., Cavenago, F., and Wittig, A., "Differential Algebra software library with automatic code generation for space embedded applications," *2018 AIAA Information Systems-AIAA Infotech Aerospace*, 2018. https://doi.org/10.2514/6.2018-0398.